# Cascade emission in electron beam ion trap plasma of $W^{25+}$ ion

V. Jonauskas[a,*], T. Pütterich[b], S. Kučas[a], Š. Masys[a], A. Kynienė[a], G. Gaigalas[a], R. Kisielius[a], L. Radžiūtė[a], P. Rynkun[a], G. Merkelis[a]

[a] *Institute of Theoretical Physics and Astronomy, Vilnius University, A. Goštauto 12, LT-01108 Vilnius, Lithuania*
[b] *Max–Planck–Institut für Plasmaphysik, EURATOM Association, D–85748 Garching, Germany*

**Abstract**

Spectra of the $W^{25+}$ ion are studied using the collisional-radiative model (CRM) with an ensuing cascade emission. It is determined that the cascade emission boosts intensities only of a few lines in the $10 - 30$ nm range. The cascade emission is responsible for the disappearance of structure of lines at about 6 nm in the electron beam ion trap plasma. Emission band at 4.5 to 5.3 nm is also affected by the cascade emission. The strongest lines in the CRM spectrum correspond to $4d^9 4f^4 \rightarrow 4f^3$ transitions, while $4f^2 5d \rightarrow 4f^3$ transitions arise after the cascade emission is taken into account.

*Keywords:* Electron beam ion trap, collisional-radiative modelling, cascade emission, tungsten

*Institute of Theoretical Physics and Astronomy, Vilnius University, A. Goštauto 12, LT-01108 Vilnius, Lithuania
*Email address:* `Valdas.Jonauskas@tfai.vu.lt` (V. Jonauskas)

## 1. Introduction

Tungsten emission has been intensively studied over the last few decades due to its application in fusion devices [1]. The intense lines in tungsten spectra are observed at around 5 nm (mostly of N-shell ions) where a large number of transitions from several charge states contributes to the plasma emission. This region has attracted great attention due to its importance for the plasma power balance and possible diagnostic applications. The $10-30$ nm region has been also investigated in the fusion and electron beam ion trap (EBIT) device plasma [2, 3, 4, 5, 6, 7]. In the fusion plasma, a complex structure of lines is observed in this region. Surprisingly, the EBIT spectra corresponding to the $W^{15+}$ – $W^{28+}$ ions feature only a few lines in the $13-18$ nm wavelength range [5]. The emission from many tungsten ions contributes to the line of sight measurements in the fusion plasma, thus, such spectra contain many lines from the different ions. On the other hand, the EBIT devices provide an unique opportunity to study the emission from one or several neighboring ions. Therefore, analysis of their spectra is much easier compared with those from other plasma sources. The emission originating only from several ions can be the reason why the EBIT spectra are sparse of the lines in the $13-18$ nm range. However, the corona modeling of the spectral line intensities provides complex structure of the lines for $W^{25+}$ [8] in the aforementioned range. Since these calculations contradict the EBIT observations, it is necessary to check what kind of spectra corresponds to the collisional-radiative modeling (CRM). On the other hand, it is shown that the cascade emission boosts the intensities only for some lines of the $W^{13+}$ ion in the EBIT plasma [9]. It has to be noted that the term "cascade emission" is used here instead of the radiative cascade in order to distinguish population of the levels from the higher-lying levels through the radiative cascade which is accounted in the corona model. The different population mechanisms appear on the scene in these two cases [9]. The cascade processes were mostly studied for the radiative and Auger decays when an inner-shell vacancy was created [10, 11, 12, 13].

Ions in the EBIT move in cycloidal orbits spending part of their time outside electron beam [14]. The cascade emission starts when the ions leave the electron beam and the interaction with the electrons ends. This effect is more pronounced for the ions in the low or intermediate ionization stages [15]. It was found that under the same conditions, the higher charge ions show less expansion in the radial direction. When the charge state of the ions increases, the Coulomb's attraction force directed toward the electron beam also increases. It leads to the decrease of the time the ions spend outside the beam where the cascade emission depopulates the excited levels. The effective electron density is often introduced in order to reduce electron-impact collision rates [15, 16]. The time fraction which the ions spend inside and outside the electron beam depends on many parameters, such as ion temperature, electron beam energy, electron beam current, electric and magnetic fields. On the other hand, the range of the ion radius $r_i$ ratio against the geometric electron radius $r_e$ can be expressed through the effective charge $Z_{eff}$ of the ion: $1/(Z_{eff}/Z)^{\alpha}$ with $1 < \alpha \leqslant 2$ [15]. For $W^{25+}$, one can estimate that the main paths of the ions span outside the electron beam: $r_i/r_e \approx 3^{\alpha}$.

The main aim of the current work is to study the emission spectra of the $W^{25+}$ ion in the EBIT plasma by performing the CRM with ensuing cascade emission. The emission from $W^{25+}$ has not deserved wide attention so far since calculations are complicated due to the open $f$ shells. Systems with the open $f$ shells is further of interest for the study of the complex multi-electron high-Z ions. The present work focuses on the $2 - 30$ nm region which accumulates the main emission from the $W^{25+}$ ion [8]. As far as we know, influence of the cascade emission on the formation of lines in the EBIT plasma has not been studied for this ion before. Previous works concentrated on analysis of the spectral lines obtained from the CRM or the corona model [3, 8]. It was shown that the corona model is suitable for the low density EBIT plasma [17]. The CRM calculations included the $4f^3$ and $4f^25l$ $(l = 0, 1, 2, 3)$ configurations but omitted the important the $4d^94f^4$ and $4f^25g$ configurations [3]. Only the strongest lines were presented in their work. The current study has been extended to 19612 levels compared with 13937 levels used in the corona model calculations [8].

The rest of the paper is organized as follows. In the next section we present theoretical methods used to calculate atomic data and emission spectra. In Section 3, the determined emission spectra corresponding to the CRM and the cascade emission are discussed.

## 2. Theoretical methods

Energy levels, radiative transition probabilities, and electron-impact excitation rates for $W^{25+}$ have been calculated using Flexible Atomic Code (FAC) [18] which implements the relativistic Dirac-Fock-Slater method. Previous study included 22 configurations [8] while the current work employs 43 configurations: $4f^3$, $4f^25l$ ($l = 0,1,2,3,4$), $4f^26l'$, $4f^27l'$ ($l' = 0,1,2,3,4,5$), $4f^28l$, $4d^94f^4$, $4d^94f^35l''$ ($l'' = 0,1,2$), $4d^94f^25s^2$, $4d^84f^5$, $4f5s^2$, $4f5s5l'''$ ($l''' = 1,2,3,4$), $4f5p^2$, $4f5p5d$, $4f5s6l$, $4p^54f^4$, $4p^54f^35s$. These configurations produce 19612 levels. Configuration interaction has been taken into account for all the considered configurations. The radiative transition probabilities have been calculated for electric dipole, quadrupole, and octupole and for magnetic dipole and quadrupole transitions.

Electron-impact excitation cross-sections are obtained within the distorted wave approximation. Collision rates are calculated for 790 eV electron beam energy which corresponds to the energy used in the spectra measurements [5]. The Gaussian distribution function with a full width at a half-maximum of 30 eV is used for the electron energy.

Populations of levels in the CRM have been obtained by solving the system of coupled rate equations

$$\frac{dn_i(t)}{dt} = N_e \sum_k n_k(t) C_{ki} + \sum_{k>i} n_k(t) A^r_{ki} - N_e n_i(t) \sum_k C_{ik} - n_i(t) \sum_{j<i} A^r_{ij} \quad (1)$$

in the steady-state equilibrium approximation ($\frac{dn_i}{dt} = 0$). Here $n_i$ is the population of the level $i$, $A^r_{ij}$ is the radiative transition probability from the level $i$ to the level $j$, and $C_{ik}$ is the electron-impact excitation rate from the level $i$ to the level $k$, $N_e$ is the electron density ($N_e = 1 \times 10^{12}$ cm$^{-3}$).

Total populations of the levels during the cascade emission can be found by summation of the population in every step of the cascade:

$$n_i^{j+1} = \sum_{m>i} \frac{n_m^j A^r_{mi}}{\sum_{k<m} A^r_{mk}}, \quad (2)$$

where $n_i^j$ corresponds to the population of the level $i$ in $j$ step of the cascade. By the step of the cascade, we mean all possible radiative transitions from every not zero-populated level to the other levels. Thus, transfer of the population through the intermediate levels is not included in the single step. Equation (2) means that radiative transition from the level $m$ to the level $i$ transfers only part $A^r_{mi}/\sum_{k<m} A^r_{mk}$ of the population $n_m^j$. The same approach was used analyzing Auger cascades [10, 12, 13]. Since the cascade emission takes place after ions leave electron beam, the initial population of the levels for the first step of the cascade is determined from the CRM.

Equation (2) determines the populations of the levels when all the higher-lying levels are depopulated by the radiative decay. However, fraction of depopulation strongly depends on the time which the ions spend outside the electron beam. In this case, the population of the levels has to be determined by solving the time-dependent rate equations which omits interaction with the electrons:

$$\frac{dn_i(t)}{dt} = \sum_{k>i} n_k(t) A^r_{ki} - n_i(t) \sum_{j<i} A^r_{ij}. \tag{3}$$

The total population $n_i(\Delta t)$ which leaves the level $i$ during the time interval $\Delta t$ is found by integrating expression:

$$\frac{dn_i(t)}{dt} = n_i(t) \sum_{j<i} A^r_{ij} \tag{4}$$

which leads to

$$n_i(\Delta t) = \int_0^{\Delta t} \frac{dn_i(t)}{dt} dt = \int_0^{\Delta t} n_i(t) dt \sum_{j<i} A^r_{ij}. \tag{5}$$

Here $\Delta t$ is the time the ions have spent outside the electron beam. Equation (5) provides the populations for the time-integrated line intensities. The total population obtained by summation of the population from every step of the cascade in Eq. (2) corresponds to the integration taking $\Delta t = \infty$ in Eq. (5). Practically, however, convergence of the spectral line intensities has to be obtained for the finite time values. The equation (2) is applied to calculate the final spectra of the cascade emission. Thus, there is no need to perform convergence check of the spectra obtained from Eq. (5).

## 3. Results

The CRM spectrum in the $2 - 30$ nm range is presented in Fig. 1. The strongest lines correspond to the $4d^9 4f^4 \to 4f^3$ and $4f^2 5d \to 4f^3$ transitions. These lines form complex structure at about 5 nm. It has to be noted that our CRM calculations succeeded to reproduce a smaller peak in the $5.5 - 6$ nm region. The similar peak but with larger intensity was obtained for $W^{23+}$ in the CRM spectra at various electron densities using Maxwellian distribution for the electron velocities [7]. The spectra from fusion plasma contain this additional structure of the lines [2]. The following lines mainly arise from the $4d^9 4f^4 \to 4f^3$ transitions in our calculations. However, this structure is not seen in the EBIT plasma of tungsten ions [19] suggesting that some other mechanisms are responsible for the line formation.

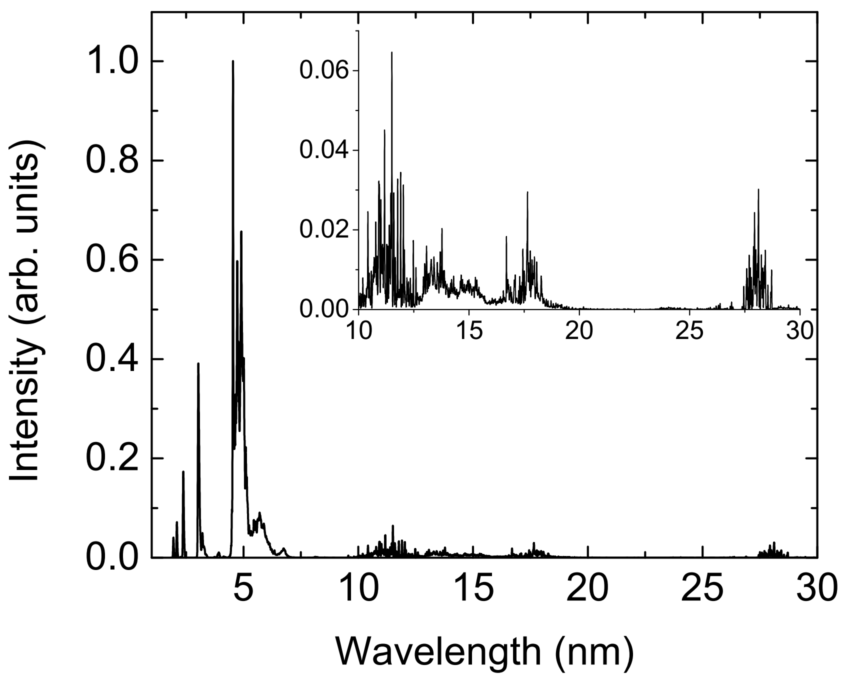


Figure 1: CRM spectrum of $W^{25+}$. The inset shows structure of lines in the range $10-30$ nm.

The current CRM calculations (Fig. 1) and the previous results from the corona model [9] present a complex structure of the emission lines in the range $10-30$ nm. In the current calculations, the number of configurations has been increased to check the influence of higher-lying levels on the formation of spectral lines. It has to be noted that the strongest lines in the spectral range arise from the $4f^25s \to 4f^3$ transitions which have wavelengths in the $10-12$ nm region. The configuration $4f^25s$ is the first excited one which can decay to the ground configuration only through the electric octupole transitions in a single-configuration approximation. Extended basis of interacting configurations makes it possible for the electric dipole transitions to occur. However, their transition probabilities are much lower than those of other electric dipole transitions in the region. Other strong lines in this region come from the $4f^25f \to 4f^25d$ ($12-16$ nm), $4f^25d \to 4f^25p$ ($12-14$, $16-18$ nm), and $4f^25p \to 4f^25s$ ($16-19$, $27-30$ nm) transitions.

Unfortunately, the EBIT spectra exhibit just a few lines in the spectral range from 13 to 18 nm [5]. As the theoretical spectra contain the complex structure of lines compared with the observations, it was suggested that

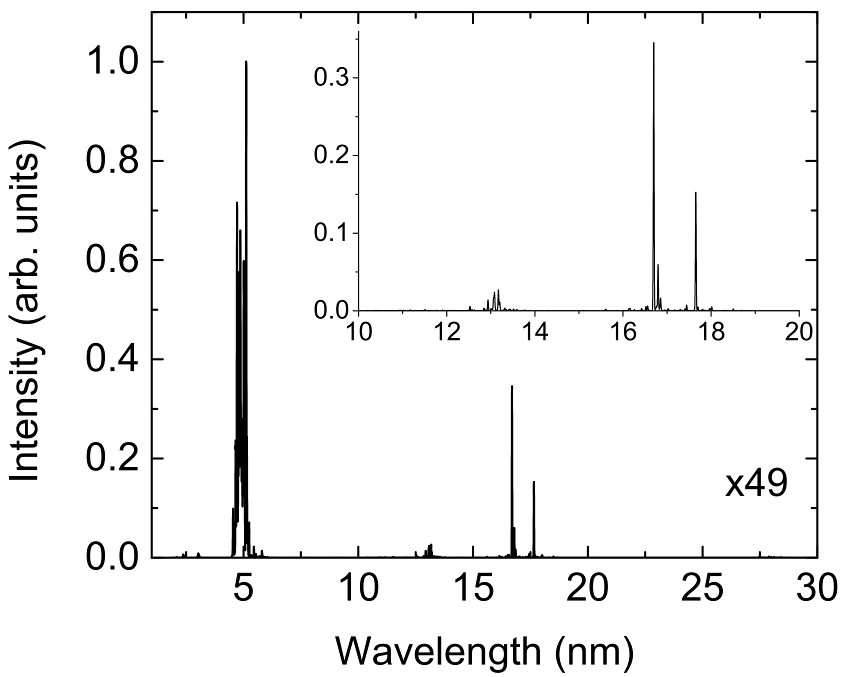


Figure 2: Cascade emission spectrum of $W^{25+}$. The inset shows structure of lines in the $10 - 20$ nm range. The factor shows an increase of the line intensities compared to the CRM spectrum.

cascade emission process, which starts after ions leave the electron beam, could be important in the formation of the spectral lines. It has been previously demonstrated that the cascade emission highlights only a few lines in the spectrum [9]. However, such an effect has been determined for the low ionization stage, $W^{13+}$. As was mentioned above, influence of the cascade emission has to be larger for the lower ionization stages compared to the intermediate charge states, which, as far as we know, have never been studied using the cascade emission process.

Figure 2 shows that the cascade emission highlights several lines in the range $10 - 30$ nm for the $W^{25+}$ ion. In this case, the population of levels is obtained using Eq. (2). In our view, the presented results demonstrate the validity of our idea that the cascade emission is responsible for line formation in the EBIT spectra. The strongest lines correspond to the $4f^25d \rightarrow 4f^25p$ and $4f^25p \rightarrow 4f^25s$ transitions in $W^{25+}$ among the levels with high $J$ values (Table 1). Due to the the significantly smaller number of such levels and selection rules for the electric dipole transitions, the cascade emission leads

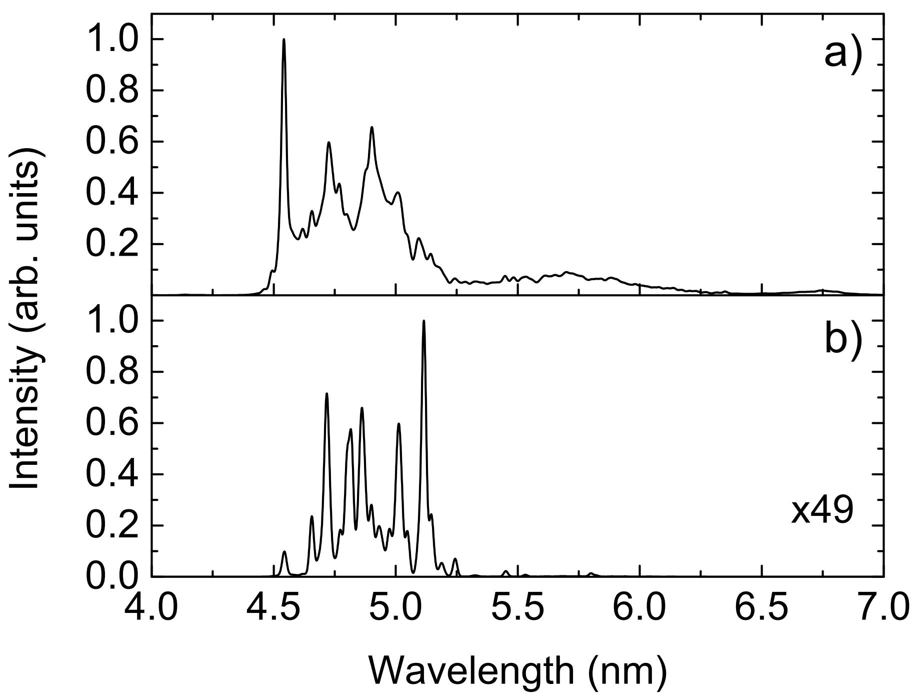


Figure 3: Theoretical spectra of the $W^{25+}$ ion obtained a) from the CRM and b) from the CRM with ensuing emission cascade [Eq. (2)] in the $4-7$ nm spectral range. The factor shows an increase of the line intensities compared to the CRM spectrum.

to the concentration of intensity.

The EBIT experiment for the $W^{25+}$ ion also contains a few strong lines but with shorter wavelengths by about 2 nm compared with our calculations. The discrepancy between the theoretical and experimental wavelengths shows that important correlation effects are not taken into account for the $4f^25d \to 4f^25p$ and $4f^25p \to 4f^25s$ transitions. The importance of the correlation effects for tungsten ions has been illustrated for magnetic dipole transitions [20, 21] using configuration interaction strength [22, 23] to build basis of the interacting configurations. However, these calculations are very cumbersome. Furthermore, for Er-like tungsten it was found that FAC can show discrepancy for wavelengths within 2 nm of the measured values when the correlation effects are not considered [24].

It has to be noted that influence of the $4f^25s \to 4f^3$ transitions on the line formation is negligible in the cascade emission spectrum. The corona model has revealed that intensities of these lines strongly increase due to contributions of the higher-lying levels through radiative cascade [8].

The relative intensities of the lines in the $4-7$ nm region compared with the lines at the shorter wavelength side are strongly increased in the cascade emission spectrum (Fig. 2) compared with the CRM spectrum (Fig. 1). These lines in the $2-4$ nm range originate from the $4f^25g \to 4f^3$, $4f^26g \to 4f^3$, $4f^27g \to 4f^3$, and $4f^28g \to 4f^3$ transitions. The previous investigation showed that strong electron-impact excitations occur from the ground configuration to the $4f^25g$ and $4f^26g$ configurations [8]. Populations of these configurations are not affected by the cascade emission process because the $4f^25g$, $4f^26g$, $4f^27g$, and $4f^28g$ configurations are highly excited ones. The cascade emission is responsible for increase of the spectral line intensities at 5 nm.

Other interesting result of modeling is formation of lines in the $4.5-5.3$ nm region (Fig. 3). It seems that the structure of these lines is not so significantly affected by the cascade emission as in the $13-18$ nm range because the emission lines overlap in the CRM and cascade emission spectra. However, it can be seen from Fig. 3 that the cascade emission spectrum is more structured than the CRM one and distribution of the line intensities is different. The CRM calculations show that the lines in the $4.5-5.3$ nm region correspond to the $4d^94f^4 \to 4f^3$ and $4f^25d \to 4f^3$ transitions. Nevertheless, other levels are involved in the line formation for the cascade emission spectrum compared to the CRM calculations. Figure 4 shows how line intensities in the region changes with time. It can be seen that many strong lines disappear from the spectrum while the other line intensities are significantly increased. The strongest lines in the CRM spectrum correspond to the $4d^94f^4 \to 4f^3$ transitions (Table 2) while the $4f^25d \to 4f^3$ transitions dominate in the cascade emission spectrum (Table 3). One can see that the distribution of the line intensities in the CRM calculations is more smooth compared with the cascade emission data. There are only a few strong lines in the cascade emission spectrum.

The spectral feature of lower intensity is visible at about 5.5 nm to 6 nm in the CRM spectrum but it is not seen in the cascade emission calculations. This additional lower intensity peak is presented in the fusion spectra [2] but it disappears from the EBIT spectra [19]. The obtained results illustrate importance of the cascade emission of ions outside the electron beam in the EBIT device. To the best of our knowledge, these differences in the fusion and EBIT spectra have not been explained before. It has to be noted that group of lines in $5.5-6.0$ nm region seen in the CRM spectrum disappears from

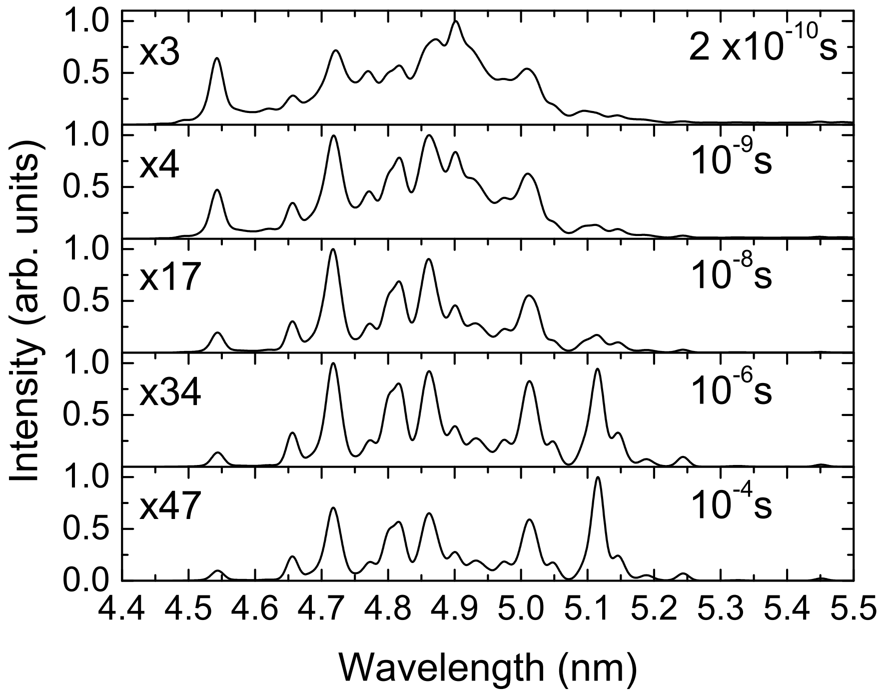


Figure 4: Time-integrated spectra of cascade emission in the $4.4 - 5.5$ nm region. Times spent by ions outside the elecron beam are shown. The factor shows an increase of the line intensities compared to the CRM spectrum.

the cascade emission spectrum after about $10^{-8}$ s. The relative intensities of the lines decrease about two times after $2 \cdot 10^{-10}$ s and four times after $10^{-9}$ s compared to the intensity of the strongest line in the spectrum. Since this group of lines is not seen in the EBIT spectrum it implies that the ions spend outside the beam in average more than $10^{-9}$ s.

In addition, we have estimated influence of charge exchange process on formation of spectral lines due to interaction with neutrals. The captured electron occupies a state with principal quantum number $n_c \approx Z_{eff}^{3/4}$ ($Z_{eff}$ is the effective charge of the ion) [25]. For the $W^{26+}$ ion, one can derive $n_c \approx 12$. The angular momentum of the captured electron is defined by the ion charge and the relative collision velocity $v$ (in atomic units): $l = (5Z_{eff})^{0.5}v$ [25]; that leads to $l = 0$ for the considered collision energy. Again, the cascade emission from the $4f^2 12s$ configuration gives a large number of the lines in the $13 - 18$ nm range. It indicates that the charge exchange process is not important for the formation of the spectral lines from the $W^{25+}$ ion in the

EBIT plasma. The same result was obtained for the $W^{13+}$ ion [9] and for the higher ionization stages of the tungsten ions [26, 27].

## 4. Conclusions

The CRM with ensuing cascade emission have been studied for the $W^{25+}$ ion. It is demonstrated that the cascade emission is responsible for formation of some lines in the EBIT spectra of the $W^{25+}$ ion. These lines correspond to transitions among the levels with high $J$ values.

The relative intensity of lines at 5 nm is strongly increased in the cascade emission spectrum compared to the lines at the shorter wavelength side which are not affected by the cascade emission. The cascade emission produces only a few strong lines in the region while the CRM calculations give more smooth distribution for the line intensities. The strongest lines in the CRM spectrum correspond to the $4d^9 4f^4 \to 4f^3$ transitions while many lines from the $4f^2 5d \to 4f^3$ transitions appear in the cascade emission calculations.

The CRM gives a spectrum with a complex structure of lines in the $13 - 18$ nm region contradicting the observations as well as cascade emission spectrum. Calculations show that the lines belong to the $4f^2 5d \to 4f^2 5p$ and $4f^2 5p \to 4f^2 5s$ transitions.

The less intense line structure observed in fusion spectra at about 6 nm is reproduced by our CRM calculations. The missing structure of the lines in the EBIT measurements is explained by the cascade emission of ions outside the electron beam. The reason of the difference between the fusion and EBIT spectra for this wavelength region has never been determined before. Time-integrated study of the line intensities gives that the ions spend in average more than $10^{-9}$ s outside the electron beam.

Finally, our results demonstrate that the cascade emission has to be taken into account for the ions in intermediate ionization stages when the spectra from the EBIT plasma are analyzed. The CRM alone does not provide a reasonable agreement with the measurements because it omits physical processes which occur after the ions leave the electron beam region.

## Akcnowledgement

This research was funded by European Social Fund under the Global Grant Measure (No.: VP1-3.1-ŠMM-07-K-02-015).

## References


[1] Bolt H, Barabash V, Federici G, Linke J, Loarte A, Roth J, and Sato K. Plasma facing and high heat flux materials - needs for ITER and beyond. J Nucl Mater 2002; 307: 43-52.

[2] Pütterich T, Neu R, Biedermann C, Radtke R and ASDEX Upgrade Team. Disentangling the emissions of highly ionized tungsten in the range 4 - 14 nm. J Phys B: At Mol Opt Phys 2005; 38: 3071.

[3] Radtke R, Biedermann C, Fussmann G, Schwob J, Mandelbaum P and Doron R. Measured line spectra and calculated atomic physics data for highly charged tungsten ions. At Plas Mater Interac Data Fusion 2007; 13: 45.

[4] Pütterich T, Neu R, Dux R, Whiteford a D and O'Mullane M G. Modelling of measured tungsten spectra from ASDEX Upgrade and predictions for ITER. Plas Phys Contr Fusion 2008; 50: 085016.

[5] Biedermann C. Spectroscopy of highly charge ions with EBIT. ADAS Workshop 2009 `http://www.adas.ac.uk/talks2009.php` .

[6] Suzuki C, Harte C S, Kilbane D, Kato T, Sakaue H A, Murakami I, Kato D, Sato K, Tamura N, Sudo S, Goto M, D'Arcy R, Sokell E and O'Sullivan G. Interpretation of spectral emission in the 20 nm region from tungsten ions observed in fusion device plasmas. J Phys B: At Mol Opt Phys 2011; 44(17): 175004.

[7] Pütterich T, Jonauskas V, Neu R, Dux R and ASDEX Upgrade Team. The extreme ultraviolet emissions of $W^{23+}(4f^5)$ . AIP Conf Proc 2013; 1545(1): 132-142.

[8] Alkauskas A, Rynkun P, Gaigalas G, Kynienė A, Kisielius R, Kučas S, Masys Š, Merkelis G and Jonauskas V. Theoretical investigation of spectroscopic properties of $W^{25+}$. J Quant Spectrosc Radiat Transfer 2014; 136: 108-118.

[9] Jonauskas V, Masys Š, Kynienė A, Gaigalas G. Cascade emission in electron beam ion trap plasma. J Quant Spectrosc Radiat Transfer 2013; 127: 64-69.

[10] Jonauskas V, Partanen L, Kučas S, Karazija R, Huttula M, Aksela S and Aksela H. Auger cascade satellites following $3d$ ionization in xenon. J Phys B: At Mol Opt Phys 2003; 36(22): 4403-4416.

[11] Jonauskas V, Karazija R, and Kučas S. The essential role of many-electron Auger transitions in the cascades following the photoionization of $3p$ and $3d$ shells of Kr. J Phys B: At Mol Opt Phys 2008; 41(21): 215005(5pp).

[12] Palaudoux J, Lablanquie P, Andric L, Ito K, Shigemasa E, Eland J H D, Jonauskas V, Kučas S, Karazija R and Penent F. Multielectron spectroscopy: Auger decays of the krypton $3d$ hole. Phys Rev A 2010; 82(4): 043419.

[13] Jonauskas V, Kučas S and Karazija R. Auger decay of $3p$-ionized krypton. Phys Rev A 2011; 84: 053415.

[14] Gillaspy J, Aglitskiy Y, Bell E, Brown C, Chantler C, DeslattesR, Feldman U, Hudson L, Laming J, Meyer E, Morgan C, Pikin A, Roberts J, Ratliff L, Serpa F, Sugar J and Takacs E. Overview of the electron-beam ion-trap program at NIST. Phys Scr 1995; T59: 392-395.

[15] Liang G Y, Lopez-Urrutia J R C, Baumann T M, Epp S W, Gonchar A, Lapierre A, Mokler P H, Simon M C, Tawara H, Maeckel V, Yao K, Zhao G, Zou Y and Ullrich J. Experimental investigations of ion charge distributions, effective electron densities, and electron-ion cloud overlap in electron beam ion trap plasma using extreme-ultraviolet spectroscopy. Astr J 2009; 702(2): 838-850.

[16] Chen H, Beiersdorfer P, Heeter L A, Liedahl D A, Naranjo-Rivera K L, Träbert E, Gu M F and Lepson J K. Experimental and Theoretical Evaluation of Density-sensitive N VI, Ar XIV, and Fe XXII Line Ratios. Astr J 2004; 611: 598-604.

[17] Jonauskas V, Kučas S and Karazija R. On the interpretation of the intense emission of tungsten ions at about 5 nm. J Phys B: At Mol Opt Phys 2007; 40(11): 2179-2188.

[18] Gu M F. The flexible atomic code. Can J Phys 2008; 86: 675-689.

[19] Radtke R, Biedermann C, Schwob J L, Mandelbaum P and Doron R. Line and band emission from tungsten ions with charge 21+ to 45+ in the $45-70$ Å range. Phys Rev A 2001; 64(1): 012720.

[20] Jonauskas V, Kisielius R, Kynienė A, Kučas S and Norrington P H. Magnetic dipole transitions in $4d^N$ configurations of tungsten ions. Phys Rev A 2010; 81: 012506.

[21] Jonauskas V, Gaigalas G and Kučas S. Relativistic calculations for M1-type transitions in configurations of $W^{29+}$ - $W^{37+}$ ions. At Data Nucl Data Tables 2012; 98(1): 19-42 .

[22] Karazija R. Introduction to the Theory of X-Ray and Electronic Spectra of Free Atoms. New York: Plenum Press; 1996.

[23] Kučas S, Jonauskas V and Karazija R. Global characteristics of atomic spectra and their use for the analysis of spectra. IV. Configuration interaction effects. Phys Scr 1997; 55(6): 667-675.

[24] Clementson J, Beiersdorfer P, Magee E W, McLean H S and Wood R D. Tungsten spectroscopy relevant to the diagnostics of ITER divertor plasmas. J Phys B: At Mol Opt Phys 2010; 43(14): 144009.

[25] Beiersdorfer P, Olson R E, Brown G V, Chen H, Harris C L, Neill P A, Schweikhard L, Utter S B and Widmann K. X-Ray Emission Following Low-Energy Charge Exchange Collisions of Highly Charged Ions. Phys Rev Lett 2000; 85(24): 5090-5093.

[26] Ralchenko Y, Tan J N, Gillaspy J D, Pomeroy J M and Silver E. Accurate modeling of benchmark x-ray spectra from highly charged ions of tungsten. Phys Rev A 2006; 74(4): 042514.

[27] Ralchenko Y, Reader J, Pomeroy J M , Tan J N and Gillaspy J D. Spectra of $W^{39+}$-$W^{47+}$ in the 12-20 nm region observed with an EBIT light source. J Phys B: At Mol Opt Phys 2007; 40(19): 3861-3875.

Table 1: The strongest lines of the cascade emission spectrum for $W^{25+}$ in the $10-20$ nm wavelength range. Wavelengths $\lambda$, relative intensities $I$, and indexes of initial $i$ and final $f$ levels are presented. $J$ stands for the total angular momentum quantum number.

| $\lambda$ (nm) | $I$ | $i$ | $f$ | $J_i$ | $J_f$ | Initial level | Final level |
|---|---|---|---|---|---|---|---|
| 16.698 | 100 | 1094 | 107 | 17/2 | 15/2 | $4f_{7/2}^2$ (6) $5d_{5/2}^1$ | $4f_{7/2}^2$ (6) $5p_{3/2}^1$ |
| 17.653 | 54 | 107 | 51 | 15/2 | 13/2 | $4f_{7/2}^2$ (6) $5p_{3/2}^1$ | $4f_{7/2}^2$ (6) $5s_{1/2}^1$ |
| 16.693 | 25 | 1152 | 127 | 17/2 | 15/2 | $4f_{5/2}^1$ $4f_{7/2}^1$ (6) $5d_{5/2}^1$ | $4f_{5/2}^1$ $4f_{7/2}^1$ (6) $5p_{3/2}^1$ |
| 16.796 | 21 | 1061 | 99 | 15/2 | 13/2 | $4f_{5/2}^1$ $4f_{7/2}^1$ (5) $5d_{5/2}^1$ | $4f_{5/2}^1$ $4f_{7/2}^1$ (5) $5p_{3/2}^1$ |
| 13.173 | 9 | 1029 | 76 | 15/2 | 13/2 | $4f_{7/2}^2$ (6) $5d_{3/2}^1$ (3) | $4f_{7/2}^2$ (6) $5p_{1/2}^1$ |
| 13.085 | 8 | 1003 | 69 | 13/2 | 11/2 | $4f_{5/2}^1$ $4f_{7/2}^1$ (5) $5d_{3/2}^1$ | $4f_{5/2}^1$ $4f_{7/2}^1$ (5) $5p_{1/2}^1$ |
| 16.852 | 6 | 1087 | 109 | 15/2 | 13/2 | $4f_{7/2}^2$ (6) $5d_{5/2}^1$ | $4f_{7/2}^2$ (6) $5p_{3/2}^1$ |
| 13.062 | 5 | 1038 | 76 | 15/2 | 13/2 | $4f_{7/2}^2$ (6) $5d_{3/2}^1$ | $4f_{7/2}^2$ (6) $5p_{1/2}^1$ |
| 12.937 | 5 | 1109 | 85 | 15/2 | 13/2 | $4f_{7/2}^2$ (6) $5d_{3/2}^1$ | $4f_{5/2}^1$ $4f_{7/2}^1$ (6) $5p_{1/2}^1$ |

Table 2: The strongest lines of the CRM spectrum for $W^{25+}$ in the $4-7$ nm wavelength range. Wavelengths $\lambda$, relative intensities $I$, and indexes of initial $i$ and final $f$ levels are presented. $J$ stands for the total angular momentum quantum number.

| $\lambda$ (nm) | $I$ | $i$ | $f$ | $J_i$ | $J_f$ | Initial level | Final level |
|---|---|---|---|---|---|---|---|
| 4.546 | 100 | 1221 | 31 | 15/2 | 17/2 | $4d^3_{3/2}$ (3/2) $4f^2_{5/2}$ (2) 3/2 $4f^2_{7/2}$ (6) | $4f^1_{5/2}$ $4f^2_{7/2}$ (6) |
| 4.656 | 99 | 1200 | 31 | 17/2 | 17/2 | $4d^3_{3/2}$ (3/2) $4f^2_{5/2}$ (4) 5/2 $4f^2_{7/2}$ (6) | $4f^1_{5/2}$ $4f^2_{7/2}$ (6) |
| 4.543 | 91 | 1186 | 6 | 13/2 | 15/2 | $4d^3_{3/2}$ (3/2) $4f^1_{5/2}$ (1) $4f^3_{7/2}$ (15/2) | $4f^1_{5/2}$ $4f^2_{7/2}$ (6) |
| 4.544 | 91 | 1176 | 3 | 11/2 | 13/2 | $4d^3_{3/2}$ (3/2) $4f^2_{5/2}$ (4) 5/2 $4f^2_{7/2}$ (6) | $4f^1_{5/2}$ $4f^2_{7/2}$ (6) |
| 4.536 | 87 | 1204 | 13 | 11/2 | 13/2 | $4d^3_{3/2}$ (3/2) $4f^3_{5/2}$ (9/2) 3 $4f^1_{7/2}$ | $4f^2_{5/2}$ (4) $4f^1_{7/2}$ |
| 4.539 | 84 | 1220 | 27 | 11/2 | 13/2 | $4d^3_{3/2}$ (3/2) $4f^2_{5/2}$ (4) 5/2 $4f^2_{7/2}$ (4) | $4f^1_{5/2}$ $4f^2_{7/2}$ (4) |
| 4.543 | 82 | 1209 | 18 | 13/2 | 15/2 | $4d^3_{3/2}$ (3/2) $4f^1_{5/2}$ (1) $4f^3_{7/2}$ (15/2) | $4f^2_{5/2}$ (4) $4f^1_{7/2}$ |
| 4.544 | 79 | 1219 | 29 | 13/2 | 15/2 | $4d^3_{3/2}$ (3/2) $4f^1_{5/2}$ (1) $4f^3_{7/2}$ (15/2) | $4f^1_{5/2}$ $4f^2_{7/2}$ (6) |
| 4.727 | 78 | 1137 | 13 | 13/2 | 13/2 | $4d^3_{3/2}$ (3/2) $4f^3_{5/2}$ (9/2) 4 $4f^1_{7/2}$ | $4f^2_{5/2}$ (4) $4f^1_{7/2}$ |
| 4.682 | 75 | 1188 | 29 | 15/2 | 15/2 | $4d^3_{3/2}$ (3/2) $4f^1_{5/2}$ (1) $4f^3_{7/2}$ (15/2) | $4f^1_{5/2}$ $4f^2_{7/2}$ (6) |
| 4.701 | 72 | 1160 | 18 | 15/2 | 15/2 | $4d^3_{3/2}$ (3/2) $4f^3_{5/2}$ (9/2) 4 $4f^1_{7/2}$ | $4f^2_{5/2}$ (4) $4f^1_{7/2}$ |
| 4.721 | 68 | 1174 | 27 | 13/2 | 13/2 | $4d^3_{3/2}$ (3/2) $4f^2_{5/2}$ (4) 5/2 $4f^2_{7/2}$ (4) | $4f^1_{5/2}$ $4f^2_{7/2}$ (4) |
| 4.539 | 66 | 1167 | 1 | 9/2 | 11/2 | $4d^3_{3/2}$ (3/2) $4f^3_{5/2}$ (9/2) 3 $4f^1_{7/2}$ | $4f^2_{5/2}$ (4) $4f^1_{7/2}$ |
| 4.733 | 65 | 1121 | 6 | 15/2 | 15/2 | $4f^2_{7/2}$ (6) $5d^1_{3/2}$ | $4f^1_{5/2}$ $4f^2_{7/2}$ (6) |
| 4.738 | 59 | 1183 | 34 | 11/2 | 11/2 | $4d^3_{3/2}$ (3/2) $4f^1_{5/2}$ (1) $4f^3_{7/2}$ (11/2) | $4f^3_{7/2}$ (11/2) |
| 4.727 | 55 | 1095 | 3 | 13/2 | 13/2 | $4f^1_{5/2}$ $4f^1_{7/2}$ 4 $5d^1_{3/2}$ | $4f^1_{5/2}$ $4f^2_{7/2}$ (6) |
| 4.572 | 51 | 1203 | 12 | 9/2 | 11/2 | $4d^3_{3/2}$ (3/2) $4f^2_{5/2}$ (4) 5/2 $4f^2_{7/2}$ (6) | $4f^1_{5/2}$ $4f^2_{7/2}$ (6) |
| 4.524 | 49 | 1223 | 34 | 9/2 | 11/2 | $4d^3_{3/2}$ (3/2) $4f^1_{5/2}$ (1) $4f^3_{7/2}$ (11/2) | $4f^3_{7/2}$ (11/2) |
| 4.751 | 47 | 1054 | 1 | 11/2 | 11/2 | $4d^3_{3/2}$ (3/2) $4f^3_{5/2}$ (9/2) (4) $4f^1_{7/2}$ | $4f^2_{5/2}$ (4) $4f^1_{7/2}$ |
| 5.116 | 44 | 989 | 31 | 19/2 | 17/2 | $4d^3_{3/2}$ (3/2) $4f^2_{5/2}$ (4) (7/2) $4f^2_{7/2}$ (6) | $4f^1_{5/2}$ $4f^2_{7/2}$ (6) |

Table 3: The strongest lines of the cascade emission spectrum for $W^{25+}$ in the $4-7$ nm wavelength range. Wavelengths $\lambda$, relative intensities $I$, and indexes of initial $i$ and final $f$ levels are presented. $J$ stands for the total angular momentum quantum number.

| $\lambda$ (nm) | $I$ | $i$ | $f$ | $J_i$ | $J_f$ | Initial level | Final level |
|---|---|---|---|---|---|---|---|
| 5.116 | 100 | 989 | 31 | 19/2 | 17/2 | $4d^3_{3/2}$ (3/2) $4f^2_{5/2}$ (4) 7/2 $4f^2_{7/2}$ (6) | $4f^1_{5/2}$ $4f^2_{7/2}$ (6) |
| 4.716 | 62 | 1121 | 6 | 15/2 | 15/2 | $4f^2_{7/2}$ (6) $5d^1_{5/2}$ | $4f^1_{5/2}$ $4f^2_{7/2}$ (6) |
| 4.818 | 52 | 1061 | 6 | 15/2 | 15/2 | $4f^1_{5/2}$ $4f^1_{7/2}$ 5 $5d^1_{5/2}$ | $4f^1_{5/2}$ $4f^2_{7/2}$ (6) |
| 4.800 | 43 | 1152 | 31 | 19/2 | 17/2 | $4f^1_{5/2}$ $4f^1_{7/2}$ 6 $5d^1_{5/2}$ | $4f^1_{5/2}$ $4f^2_{7/2}$ (6) |
| 4.864 | 37 | 1029 | 6 | 15/2 | 15/2 | $4f^2_{7/2}$ (6) $5d^1_{3/2}$ | $4f^1_{5/2}$ $4f^2_{7/2}$ (6) |
| 5.007 | 29 | 1038 | 27 | 15/2 | 13/2 | $4f^2_{7/2}$ (6) $5d^1_{3/2}$ | $4f^1_{5/2}$ $4f^2_{7/2}$ (4) |
| 4.856 | 26 | 1087 | 18 | 15/2 | 15/2 | $4f^2_{7/2}$ (6) $5d^1_{5/2}$ | $4f^2_{5/2}$ (4) $4f^1_{7/2}$ |
| 4.656 | 25 | 1200 | 31 | 17/2 | 17/2 | $4d^3_{3/2}$ (3/2) $4f^2_{5/2}$ (4) 5/2 $4f^2_{7/2}$ (6) | $4f^1_{5/2}$ $4f^2_{7/2}$ (6) |
| 4.727 | 23 | 1095 | 3 | 13/2 | 13/2 | $4f^1_{5/2}$ $4f^1_{7/2}$ 4 $5d^1_{5/2}$ | $4f^1_{5/2}$ $4f^2_{7/2}$ (6) |
| 5.147 | 23 | 899 | 6 | 17/2 | 15/2 | $4d^3_{3/2}$ (3/2) $4f^3_{5/2}$ (9/2) 5 $4f^1_{7/2}$ | $4f^1_{5/2}$ $4f^2_{7/2}$ (6) |
| 5.014 | 22 | 956 | 6 | 17/2 | 15/2 | $4d^3_{3/2}$ (3/2) $4f^2_{5/2}$ (4) 7/2 $4f^2_{7/2}$ (6) | $4f^1_{5/2}$ $4f^2_{7/2}$ (6) |
| 5.024 | 21 | 1029 | 27 | 15/2 | 13/2 | $4f^2_{7/2}$ (6) $5d^1_{3/2}$ | $4f^1_{5/2}$ $4f^2_{7/2}$ (4) |
| 5.106 | 18 | 956 | 18 | 17/2 | 15/2 | $4d^3_{3/2}$ (3/2) $4f^2_{5/2}$ (4) 7/2 $4f^2_{7/2}$ (6) | $4f^2_{5/2}$ (4) $4f^1_{7/2}$ |
| 5.048 | 17 | 1018 | 29 | 17/2 | 17/2 | $4d^3_{3/2}$ (3/2) $4f^1_{5/2}$ 1 $4f^3_{7/2}$ (15/2) | $4f^1_{5/2}$ $4f^2_{7/2}$ (6) |
| 4.901 | 16 | 1109 | 31 | 15/2 | 17/2 | $4f^2_{7/2}$ (6) $5d^1_{3/2}$ | $4f^1_{5/2}$ $4f^2_{7/2}$ (6) |
| 4.701 | 15 | 1160 | 18 | 15/2 | 15/2 | $4d^3_{3/2}$ (3/2) $4f^3_{5/2}$ (9/2) 4 $4f^1_{7/2}$ | $4f^2_{5/2}$ (4) $4f^1_{7/2}$ |
| 4.773 | 13 | 1087 | 6 | 15/2 | 15/2 | $4f^2_{7/2}$ (6) $5d^1_{5/2}$ | $4f^1_{5/2}$ $4f^2_{7/2}$ (6) |
| 5.094 | 10 | 949 | 13 | 15/2 | 13/2 | $4d^3_{3/2}$ (3/2) $4f^1_{5/2}$ (4) 7/2 $4f^2_{7/2}$ (4) | $4f^2_{5/2}$ (4) $4f^1_{7/2}$ |
| 4.975 | 8 | 1061 | 27 | 15/2 | 13/2 | $4f^1_{5/2}$ $4f^1_{7/2}$ 5 $5d^1_{5/2}$ | $4f^1_{5/2}$ $4f^2_{7/2}$ (4) |
| 5.244 | 8 | 899 | 18 | 17/2 | 15/2 | $4d^3_{3/2}$ (3/2) $4f^3_{5/2}$ (9/2) 5 $4f^1_{7/2}$ | $4f^2_{5/2}$ (4) $4f^1_{7/2}$ |